crystals

MDPI

Article

Prussian Blue Analogue Mesoframes for Enhanced Aqueous Sodium-ion Storage

Huiyun Sun, Wei Zhang * and Ming Hu *

School of Physics and Materials Science, East China Normal University, Shanghai 200241, China; Shyunyun16@163.com

* Correspondence: weizhang1990@163.com (W.Z.); mhu@phy.ecnu.edu.cn (M.H.); Tel.: +86-21-5434-5338

Received: 24 November 2017; Accepted: 3 January 2018; Published: 7 January 2018

Abstract: Mesostructure engineering is a potential avenue towards the property control of coordination polymers in addition to the traditional structure design on an atomic/molecular scale. Mesoframes, as a class of mesostructures, have short diffusion pathways for guest species and thus can be an ideal platform for fast storage of guest ions. We report a synthesis of Prussian Blue analogue mesoframes by top-down etching of cubic crystals. Scanning and transmission electron microscopy revealed that the surfaces of the cubic crystals were selectively removed by HCl, leaving the corners, edges, and the cores connected together. The mesoframes were used as a host for the reversible insertion of sodium ions with the help of electrochemistry. The electrochemical intercalation/de-intercalation of Na^+ ions in the mesoframes was highly reversible even at a high rate (166.7 C), suggesting that the mesoframes could be a promising cathode material for aqueous sodium ion batteries with excellent rate performance and cycling stability.

Keywords: Prussian Blue analogue; mesoframe; aqueous sodium ion battery

1. Introduction

Coordination polymers, for instance, metal-organic frameworks (MOFs) or porous coordination polymers (PCPs), are molecular solids assembled by metal ions/clusters and ligands [1–10]. The physical/chemical properties of coordination polymers, including the packing ordering of their component ions/molecules, are known to be determined by their structures [3,5,11,12]. Therefore, the most widely used approach for the property regulation of coordination polymers is structure design via manipulation of the atomic/molecular packing by intermolecular interactions [13–15]. Besides the great success achieved on the molecular/atomic scale, the structure design on a mesoscale (10~1000 nm) has recently been recognized as a promising choice [16–19]. By downsizing of a bulk crystal, the volume ratio of the surface units to the bulk units can be increased significantly, leading to a coupling effect from the bulk structure and the surface units [17,20,21]. For instance, the meso-sized coordination polymers can accommodate guest molecules still, but their phase-change type would be changed owing to the suppressing effect of the surface energy [14,22–24]. Downsizing can also shorten the diffusion distance when the guest molecules/ions travel inside, leading to high-rate adsorption/desorption ability.

Mesoframe represents a kind of mesostructures with open holes on each surface of a cube (Figure 1a). Comparing with the solid cubes, the open frames can provide larger accessible surfaces and shorter diffusion distances for guest species [25–36]. Such an ability of the mesoframes can be highly desirable for hosting guest alkaline ions. Very recently, Prussian Blue analogues ($A_xM[M'(CN)_6]_y \cdot V_{1-y} \cdot nH_2O$: A = alkali metal; M, M′ = transition metals; V= M′(CN) vacancy; $0 \leq x \leq 2$; $0 < y \leq 1$), as a kind of coordination frameworks, have been recognized as an emerging class of energy storage materials because of their exceptional capability for hosting alkali metal ions

(Figure 1b) [37–46]. In particular, Prussian Blue analogues have interstitial sites that are quite suitable for the alkali metal ions with a larger radius than that of the Li^+ ions and thus can be used as electrodes for a new generation of Na-ion and K-ion batteries [47–57]. However, because of the poor electron conductivity of Prussian Blue analogues, it is necessary to make sure that Prussian Blue analogues can have a short diffusion distance for the guest ions [58–64]. Therefore, Prussian Blue analogues mesoframes are highly needed.

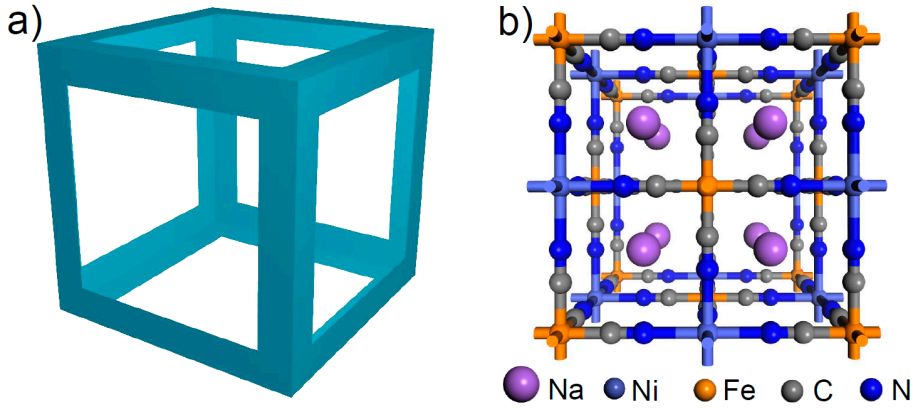

Figure 1. (**a**) Scheme for Prussian Blue analogue mesoframe. (**b**) Schematic crystal structure for Prussian Blue analogue.

The most utilized strategy for the fabrication of mesoframes is selective etching, which occurs either during the synthesis or after the formation of compounds [14,22,65–73]. For example, when Prussian Blue crystal is crystallized in hot acid under a hydrothermal condition, the disassociation occurs during the growth process. When the disassociation rate is higher than the growth rate, etching of the crystal occurs [65]. By understanding the disassociation kinetics of different parts of a crystal, post-etching becomes possible. When the location of the defects is known, a hollow cavity can be constructed inside the crystals as desired [12]. In other cases, because of the spatial-dependent reactivity, for a cubic crystal of Prussian Blue analogues, the surfaces tend to be dissolved in the acidic/basic solution quicker than the corners and edges [22,74]. Although in situ etching methods have been extensively utilized [75–79], they are not suitable for investigating the differences between solid cubes and mesoframes because of the difficulties in controlling the size/shape and composition. Alternatively, post-etching provides opportunities for comparison of the solid cubes and mesoframes with similar size/shape and composition.

Despite increased knowledge of the positive effect of mesoframes, the role of mesoframes on alkaline ion intercalation/de-intercalation in aqueous environment remains unclear. Compared to the alkaline ion intercalation/de-intercalation in organic electrodes, aqueous alkaline ion storage is safer and cheaper and thus is an indispensable solution for grid-scale energy storage [80–84]. In this work, we fabricated Prussian Blue analogue ($Na_2Ni[Fe(CN)_6]$, **1**) mesoframes by post-etching the cubic crystals. The mesoframes of **1** showed improved Na^+ ion intercalation/de-intercalation at a high rate (166.7 C).

2. Materials and Methods

2.1. Materials

Sodium hexacyanoferrate ($Na_4[Fe(CN)_6]\cdot 10H_2O$), nickel chloride hexahydrate ($NiCl_2\cdot 6H_2O$), hydrochloric acid (HCl), and trisodium citrate dihydrate ($C_6H_5Na_3O_7\cdot 2H_2O$) were purchased from Sinopharm Chemical Reagent Co. and used without further purification.

2.2. Synthesis of Cubic Crystals of ***1***

Sodium hexacyanoferrate (5 mmol, 2.425 g) was dissolved in water (250 mL) to form a clear solution (Solution A). Nickel chloride hexahydrate (2.5 mmol, 587 mg) and trisodium citrate dihydrate (12.7 mmol, 3.75 g) were dissolved in water (250 mL) to form Solution B. Solutions A and B were mixed under magnetic stirring for 5 min and then allowed to age at 25 °C for 24 h. The product was obtained after centrifugation and washed with water and ethanol several times. Finally, the cubic crystals of **1** were collected by drying at 25 °C in a vacuum oven for 24 h.

2.3. Synthesis of Mesoframes of ***1***

The cubic crystals of **1** (50 mg) were added to 20 mL of 0.4 M HCl. The solution was ultrasonicated for 1 h. Then, the product was obtained after centrifugation and washed with water and ethanol several times. Finally, the mesoframes were collected by drying at 25 °C in vacuum oven for 24 h. We noted that Fe(II) in the surfaces of the crystals was easily oxidized into Fe(III) during etching in atmosphere according to the FT-IR spectrum (Figure S8). The existence of Fe(III) in the framework changed the crystal structure from *R-3* into *Fm-3m* (Figure S9). Therefore, the powder needed to be reduced electrochemically to convert the Fe(III) into Fe(II), making sure the crystals structure of the mesoframes was *R-3* before further characterization.

2.4. Characterization

The morphology of the products was observed by a field emission scanning electron microscope (FESEM, Hitachi S-4800) (Hitachi, Tokyo, Japan) and a transmission electron microscope (TEM, JEOL JEM-2100 F) ((JEOL, Tokyo, Japan). The powder X-ray diffraction patterns were measured with a Rigaku RINT 2500 X diffractometer with Cu Kα radiation (35 kV, 25 mA). The Fourier transform infrared spectroscopy (FT-IR) spectra were obtained with a Thermo Nicolet i50.

2.5. Electrochemical Measurement

The electrochemical performance was measured using three-electrode cells. The working electrode was prepared as follows: the powder of **1** (70%), acetylene black (20%), and poly(vinylidene difluoride) (10%) were well mixed in N-methyl-2-pyrrolidone until a homogeneous slurry was formed. The slurry was then coated onto the carbon cloth with an area of 1 cm × 2 cm and was dried at 80 °C in a vacuum oven for 15 h. The mass loading of the active materials was around 2 mg cm^{-2} for each test. An Ag/AgCl electrode was used as a reference. The counter electrode contained activated carbon instead of the prepared materials, and it was also coated onto the carbon cloth. These three electrodes were immersed in the neutral solution of 1 M $NaNO_3$ and measured with the CHI 660E (Shanghai Chen Hua Instrument, Shanghai, China) electrochemical workstation.

3. Results

The crystals of **1** were synthesized by a weak-chelation-agent-assisted crystallization method [85]. Approximately, nickel chloride was mixed with tri-sodium citrate to form a green solution at first. Then, the green solution was mixed with a sodium hexacyanoferrate solution. After aging at room temperature for 24 h, the green precipitates were harvested. Scanning electron microscopy (SEM) revealed that the obtained crystals were of a cubic shape with a size ranging from 200 to 400 nm (Figure 2a). Transmission electron microscopy confirmed that the crystals were solid (Figure 2b). The cubic crystals of **1** were immersed into an HCl solution (0.4 mol L^{-1}) under continuous stirring. After 1 h, the samples were harvested by centrifugation. SEM images illustrate that the center of the surfaces of the cubic crystals was empty (Figure 2c). The corners and edges were well-retained after etching. The TEM image implies that there were solid cores inside each particle (Figure 2d). All the evidence suggests that the mesoframes of **1** were successfully obtained after post-etching the cubic

crystals. To facilitate our discussion, the cubic crystals of **1** are denoted as $\mathbf{1}_{cube}$, while the mesoframes are designated as $\mathbf{1}_{frame}$.

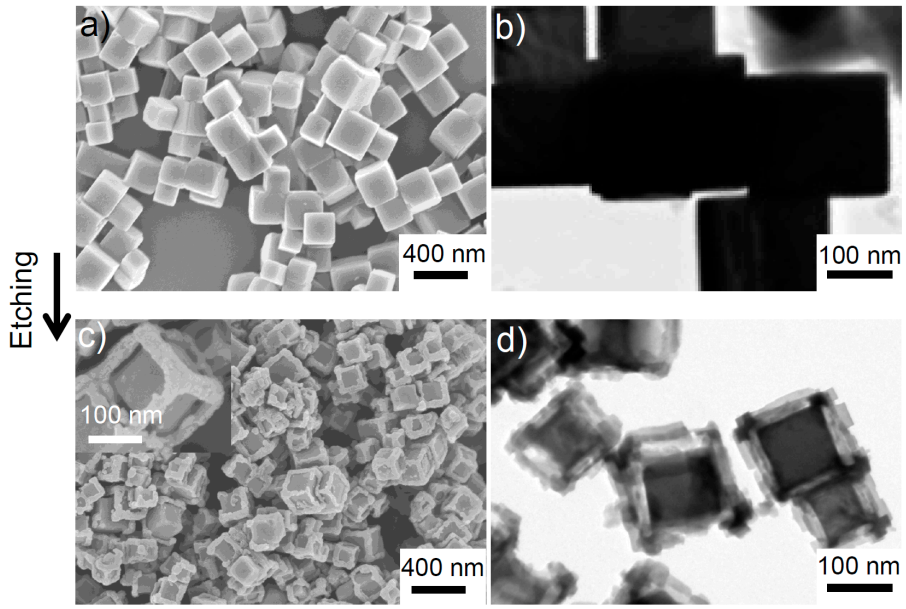

Figure 2. (**a**) SEM image of cubic crystals. (**b**) TEM image of cubic crystals. (**c**) SEM image of the product from etching of the cubic crystals. Inset is an enlarged image of a particle. (**d**) TEM image of the product from etching of the cubic crystals.

The crystal structures of $\mathbf{1}_{cube}$ and $\mathbf{1}_{frame}$ were investigated by powder X-ray diffraction (PXRD). The diffraction profiles of both samples are similar, indicating an identical crystal structure (Figure 3). The diffraction patterns can be assigned to a rhombohedral structure (*R*–3), which is typical for Prussian Blue analogues with the interstitial sites occupied by a rich amount of Na^+ ions [86]. The slight broadening of the peaks of $\mathbf{1}_{frame}$ is probably due to the lattice defects induced by etching. FT-IR spectra are shown in Figure 4. For both samples, a similar peak near 2090 cm^{-1} was observed. This band belongs to the characteristic of stretching vibration of Fe–CN–Ni [87]. Therefore, the PXRD and FT-IR investigations confirm that both $\mathbf{1}_{cube}$ and $\mathbf{1}_{frame}$ present the same crystal structure and composition, allowing us to explore the mesostructural property.

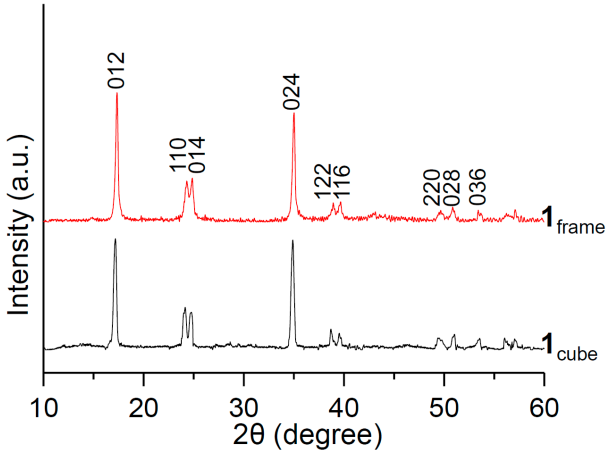

Figure 3. Powder X-ray diffraction (PXRD) patterns of **1** crystals.

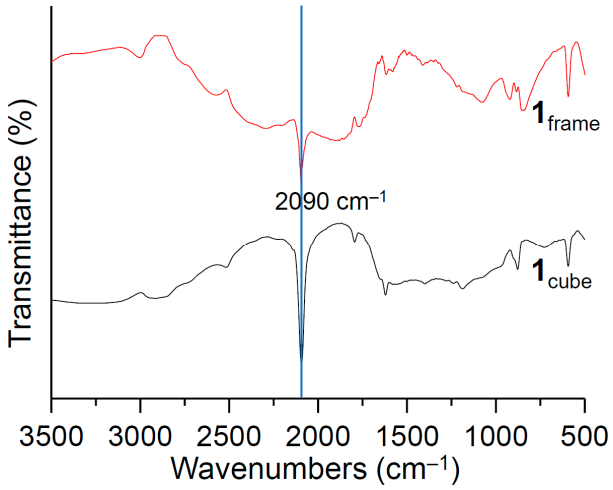

Figure 4. FT-IR spectra of **1** crystals.

To investigate the role of the frame-like mesostructure, we used the powders of **1** to host Na^+ ions. We selected an electrochemistry-controlled method to probe the Na-ion insertion/extraction amount. The crystals of **1** were used as cathodes in a three-electrode system in an $NaNO_3$ solution. In this aqueous battery system, a reversible insertion/extraction of Na^+ ions into/from the frameworks of **1** can be realized by electrochemical redox of Fe^{2+}/Fe^{3+} ions. For the storage/consumption of one electron, an Na^+ ion enters/leaves the host frameworks. Herein, we simply recorded the capacity change to understand the intercalation/de-intercalation of the Na^+ ion. The galvanostatic charge/discharge curves shown in Figure 5 present that $\mathbf{1}_{frame}$ can deliver a reversible specific capacity of 61 mAh·g^{-1} at a current density of 70 mA·g^{-1} between 0.001 to 1.0 V (vs. Ag/AgCl). The discharge curve contains a plateau at 0.3–0.6 V (vs. Ag/AgCl), corresponding to the insertion of Na^+ ions. Moreover, $\mathbf{1}_{cube}$ shows similar specific capacity (60 mAh·g^{-1}) at a current density of 70 mA·g^{-1} between 0.001 to 1.0 V (vs. Ag/AgCl). As we can see in the cyclic voltammetry (CV) curves (Figure 6), the center of the positions of redox peaks of the $\mathbf{1}_{cube}$ crystals is at around 0.4 V (vs. Ag/AgCl), and the center of the peaks of $\mathbf{1}_{frame}$ locates at around 0.36 V (vs. Ag/AgCl). The redox peaks of $\mathbf{1}_{frame}$ are much sharper corresponding to a larger quantity of the intercalated Na^+ ion in the frameworks of $\mathbf{1}_{frame}$ at this potential.

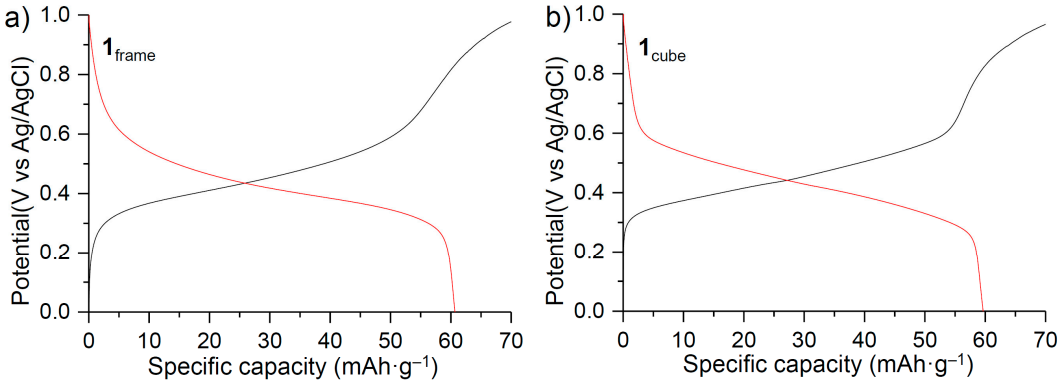

Figure 5. (**a**,**b**) Galvanostatic charge/discharge curves of $\mathbf{1}_{frame}$ and $\mathbf{1}_{cube}$ at a current density of 70 mA·g^{-1}, respectively.

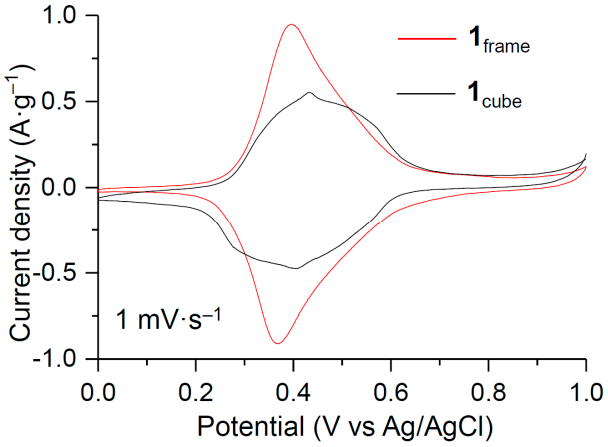

Figure 6. CV curves of **1** crystals at a scanning rate of 1 mV·s^{-1}.

We investigated the rate performance of the crystals of **1**. Figure 7 shows that $\mathbf{1}_{frame}$ and $\mathbf{1}_{cube}$ have similar capacities (approximately 60 mAh·g^{-1}) at a low current density 70 mA·g^{-1} (1 C). However, with the increase in the current rate, the capacity of $\mathbf{1}_{cube}$ decreased more drastically than the $\mathbf{1}_{frame}$. For instance, when the charge/discharge current density was as high as 10 A·g^{-1} (166.7 C), the capacity retention of $\mathbf{1}_{frame}$ was as high as 88%. However, the $\mathbf{1}_{cube}$ could only retain 41% of the initial capacity (Figure 7). The wonderful rate performance of $\mathbf{1}_{frame}$ suggests that this material could be suitable for long-term cycling. Figure 8 illustrated that $\mathbf{1}_{frame}$ could deliver a high capacity at a current density of 83.3 C (5 A·g^{-1}). The retained capacity is 94.34% of the initial capacity after 500 cycles (Figure 8). To check the performance at higher temperature, the $\mathbf{1}_{frame}$ was measured at a different current density and cycled at 5 A·g^{-1} at 40 °C (Figure S1). The rate and cycling performances, compared with performances at 25 °C, were almost unchanged. This result indicated that the rate and cycling performances were not affected at 40 °C [88].

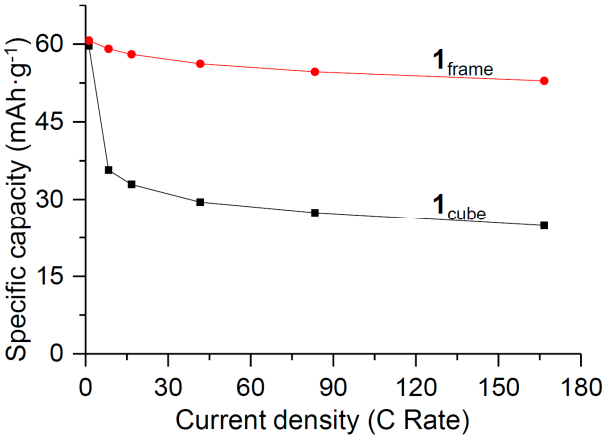

Figure 7. Rate performance of the **1** crystals.

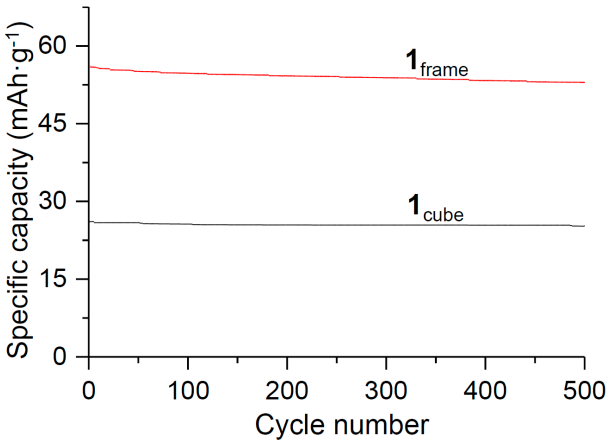

Figure 8. Cycling performance of the **1** crystals at a current density of 5 A·g^{-1}.

4. Discussion

On the basis of the relationship between the transferred electrons and the amount of the intercalated Na^+ ions, $\Delta N_e = \Delta N_{Na+}$, we converted the electrochemical data into the intercalation-deintercalation curves for Na^+ ions against the potential (vs. Ag/AgCl) (Figures 9 and 10). Apparently, both $\mathbf{1}_{cube}$ and $\mathbf{1}_{frame}$ can accommodate the same amount of Na^+ ions at a lower uptake rate, indicating that both samples have a similar capacity for the Na^+ ions (Figure 9). However, the uptake of Na^+ ions by $\mathbf{1}_{cube}$ is much lower than that by $\mathbf{1}_{frame}$ at a higher uptake rate (Figure 10). The uptake by $\mathbf{1}_{frame}$ did not decrease too much, while 50% of the uptake by $\mathbf{1}_{cube}$ was lost. Apparently, the interstitial sites in $\mathbf{1}_{frame}$ could be utilized almost completely at a high rate, while the number of the accessed interstitial sites in $\mathbf{1}_{cube}$ was significantly reduced.

There are three factors that may be affected by the meso-structure: (1) the contact between the crystal and the electrolyte; (2) the crystal structure and meso-structure change during the intercalation process; (3) the diffusion distance inside the frameworks. For Factor 1, we firstly measured the specific surface area of $\mathbf{1}_{frame}$ and $\mathbf{1}_{cube}$ by the Brunauer–Emmett–Teller (BET) method (Figure S2). The specific surface area of $\mathbf{1}_{frame}$ (59.6 m^2·g^{-1}) is close to that of $\mathbf{1}_{cube}$ (49.2 m^2·g^{-1}). Such a small difference can be ignored by considering that the crystals have to be well mixed with the conductors and electrolytes during the electrode preparation. Therefore, Factor 1 can be ignored. For Factor 2, we need to understand the structure change during the intercalation process. The ex situ PXRD analysis was carried out. For both crystals, a similar phase change between the *R-3* and *Fm-3m* structures was recorded as shown in Figures S3 and S4. The structure change is due to the accommodation and release of Na^+ ions. The shape of the two samples was also checked by SEM after 500 cycles. We noted that the meso-structures of both samples were retained (Figure S5). It should be noted that the small particles are conductive carbons that are not crystals of **1**. This result suggests that Factor 2, for the mesoframes, is not different from the cube and thus should not be considered as the reason.

Regarding Factor 3, the $\mathbf{1}_{frame}$ obviously has a shorter diffusion pathway for the Na^+ ions than that of $\mathbf{1}_{cube}$ since various parts of the crystals have been removed. For the intercalation of Na^+ ions into Prussian Blue analogues, the solvated Na^+ ions need to first be de-solvated. Then, the de-solvated Na^+ ions can enter the frameworks of the host. The entered Na^+ ions may be partially re-solvated by the mobile water molecules in the crystals during the next diffusion stage. Because re-solvation can enlarge the radius of the Na^+ ions, the diffusion of the re-solvated Na^+ ions is slower than the de-solvated Na^+ ions. Shortening the diffusion distance can likely minimize the diffusion of the re-solvated Na^+ ions and accelerate the intercalation process, leading to the utilization of the interstitial sites adequately. To confirm this point, we measured the diffusion coefficient for both samples. The diffusion coefficient of Na^+ ions can be calculated with the Randles–Sevcik equation [89]: $I_p = 2.69 \times 10^5 n^{3/2} S C_{Na} D_{Na}{}^{1/2} v^{1/2}$, where I_p is the peak current (A), n is the number of electrons transferred per molecule during the

intercalation/deintercalation procedure (n = 1 for Fe^{2+}/Fe^{3+} redox pair), S is the effective contact area between the electrode and electrolyte (here the area of the electrode = 1 cm^2), C_{Na} is the molar concentration of Na^+ ions (1.3×10^{-3} mol·cm^{-3}) [90], D_{Na} is the diffusion coefficient of Na^+ ions ($cm^2 \cdot s^{-1}$), and ν is the scan rate ($V \cdot s^{-1}$). We carried out CV scans at various scan rates from 0.2 to 1 mV s^{-1} (Figures S6a and S7a). The peak current correlates linearly to the square root of the scan rate for both samples. On the basis of the slopes received from the plots of the anodic I_p versus $\nu^{1/2}$ (Figures S6b and S7b), the calculated D_{Na} is 7.35×10^{-9} $cm^2 \cdot s^{-1}$ for $\mathbf{1}_{cube}$, and 14.0×10^{-9} $cm^2 \cdot s^{-1}$ for $\mathbf{1}_{frame}$, respectively. Apparently, the diffusion coefficient for Na^+ in $\mathbf{1}_{frame}$ is significantly larger than in $\mathbf{1}_{cube}$. The diffusion coefficient strongly relates to the moving of the Na^+ ions, including the transfer from the electrolytes to the interstitial sites and the movement among the interstitial sites. In general, the transfer part is fast, while the moving part is slow. Because the transfer part for both samples is similar owing to their close specific surface areas, the less contribution there is from the moving part, the larger the diffusion coefficient can be. The moving step in $\mathbf{1}_{frame}$ is shorter than in $\mathbf{1}_{cube}$ because of the shape of the mesoframe, indicating less contribution to the diffusion coefficient from the moving step in $\mathbf{1}_{frame}$. Therefore, the diffusion coefficient for $\mathbf{1}_{frame}$ is larger than for $\mathbf{1}_{cube}$. The larger diffusion coefficient means that the Na^+ ions can move fast and thus utilize the interstitial sites at a high current rate, leading to a larger capacity at a high current density. Therefore, we can say the short diffusion distance in $\mathbf{1}_{frame}$ enlarges the D_{Na} and is thus the apparent reason for the better rate performance of the mesoframe structure.

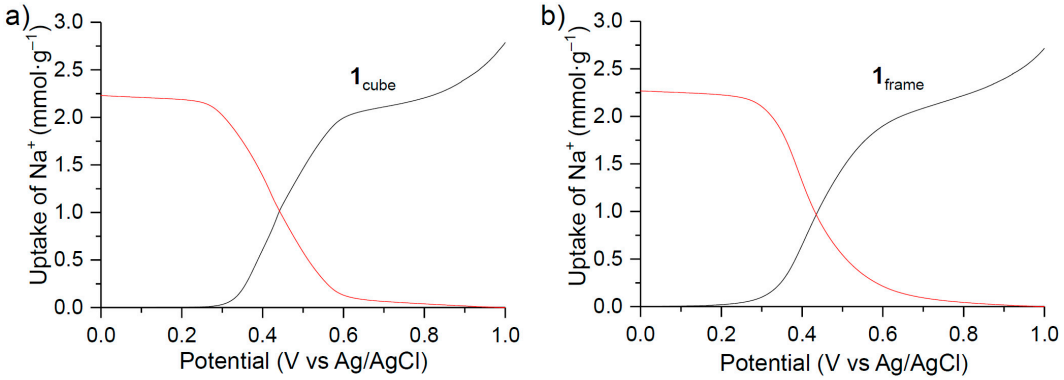

Figure 9. (**a**) Accommodation–release curves for Na^+ ions in $\mathbf{1}_{cube}$ against the potential (vs. Ag/AgCl). (**b**) Accommodation–release curves for Na^+ ions in $\mathbf{1}_{frame}$ against the potential (vs. Ag/AgCl).

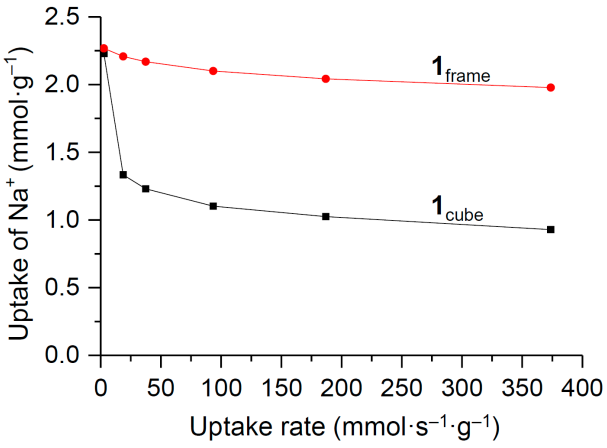

Figure 10. Uptake of Na^+ ions by **1** crystals at different uptake rates.

The above discussion suggests that the difference in Na-ion insertion/extraction at high rates for both samples can be explained as follows. At a low rate, the Na^+ ions can be inserted/extracted almost fully in/from both of the cubes and mesoframes. When the rate becomes high (for example, higher than 70 $mA \cdot g^{-1}$), Na^+ ions may be hard to access to the center part of the cubes during the insertion process, while a large percentage of the interstitial site of the mesoframes can be accessed. Therefore, the mesoframes can have a much larger specific capacity, especially at a high current rate (higher than 0.07 $A \cdot g^{-1}$), representing an excellent rate performance. In addition, as our cycling test was performed at a high current rate, the cycling stability of the mesoframes of course should be superior compared to the cubes as well.

5. Conclusions

In summary, we synthesized monocrystalline NiFe(II) Prussian Blue analogue mesoframes by a chemical etching method. This morphology significantly reduced the diffusion pathway for Na^+ ions inside the crystal, leading to fast guest ion intercalation/de-intercalation, which is hard to achieve in solid crystals. The fast guest ion accommodation ability of the crystals could be used in aqueous Na-ion batteries. Based on the mesoframes, cathodes suitable for a high-rate charging/discharging (166 C) aqueous Na-ion batteries were fabricated, and it was demonstrated that the mesoframe is a promising meso-architecture for an enhancement in the performance of coordination polymers. In addition, the impressive cycling performance of the mesoframes may be useful for grid-scale energy storage.

Supplementary Materials: The following are available online at www.mdpi.com/2073-4352/08/01/23/s1. Figure S1: Rate performance (**a**) and cycling performance (**b**) of $\mathbf{1}_{frame}$ at different temperatures; Figure S2: N_2 adsorption-desorption isotherms of **1** crystals; Figure S3: Ex situ PXRD patterns of the electrochemically active cubic crystals at charge/discharge during the first cycle at a current density of 0.07$A \cdot g^{-1}$; Figure S4: Ex situ PXRD patterns of the electrochemically active mesoframes at charge/discharge during the first cycle at a current density of 0.07$A \cdot g^{-1}$; Figure S5: (**a**) SEM of cubic crystals after cycling. (**b**) SEM of mesoframes after cycling for 500 cycles; Figure S6: (**a**) Cyclic voltammetry curves of $\mathbf{1}_{cube}$ at various scanning rates. (**b**) The anodic and cathodic peak currents as functions of the square root of scanning rates; Figure S7: (**a**) Cyclic voltammetry curves of $\mathbf{1}_{frame}$ at various scanning rates. (**b**) The anodic and cathodic peak currents as functions of the square root of scanning rates; Figure S8: FT-IR spectrum of mesoframes before electrochemical activation; Figure S9: PXRD patterns of mesoframes before electrochemical activation.

Acknowledgments: This work was supported by the National Natural Science Foundation of China (Grant No. 21401056, 21473059) and the Large Instruments Open Foundation of East China Normal University.

Author Contributions: Ming Hu and Wei Zhang conceived and designed the experiments; Huiyun Sun performed the experiments; Huiyun Sun and Ming Hu analyzed the data; Ming Hu and Huiyun Sun wrote the paper.

Conflicts of Interest: The authors declare no conflict of interest.

References

1. James, S.L. Metal-organic frameworks. *Chem. Soc. Rev.* **2003**, *32*, 276–288. [CrossRef] [PubMed]
2. Rowsell, J.L.C.; Yaghi, O.M. Metal-organic frameworks: A new class of porous materials. *Micropor. Mesopor. Mater.* **2004**, *73*, 3–14. [CrossRef]
3. Eddaoudi, M.; Kim, J.; Rosi, N.; Vodak, D.; Wachter, J.; O'Keeffe, M.; Yaghi, O.M. Systematic design of pore size and functionality in isoreticular MOFs and their application in methane storage. *Science* **2002**, *295*, 469–472. [CrossRef] [PubMed]
4. Kitagawa, S.; Kitaura, R.; Noro, S. Functional porous coordination polymers. *Angew. Chem. Int. Ed.* **2004**, *43*, 2334–2375. [CrossRef] [PubMed]
5. Chui, S.S.Y.; Lo, S.M.F.; Charmant, J.P.H.; Orpen, A.G.; Williams, I.D. A chemically functionalizable nanoporous material $[Cu_3(TMA)_2(H_2O)_3]_n$. *Science* **1999**, *283*, 1148–1150. [CrossRef] [PubMed]
6. Hwang, Y.K.; Hong, D.-Y.; Chang, J.-S.; Jhung, S.H.; Seo, Y.-K.; Kim, J.; Vimont, A.; Daturi, M.; Serre, C.; Ferey, G. Amine grafting on coordinatively unsaturated metal centers of MOFs: Consequences for catalysis and metal encapsulation. *Angew. Chem. Int. Ed.* **2008**, *47*, 4144–4148. [CrossRef] [PubMed]
7. Dan-Hardi, M.; Serre, C.; Frot, T.; Rozes, L.; Maurin, G.; Sanchez, C.; Ferey, G. A new photoactive crystalline highly porous titanium(iv) dicarboxylate. *J. Am. Chem. Soc.* **2009**, *131*, 10857–10859. [CrossRef] [PubMed]

8. Furukawa, S.; Hirai, K.; Nakagawa, K.; Takashima, Y.; Matsuda, R.; Tsuruoka, T.; Kondo, M.; Haruki, R.; Tanaka, D.; Sakamoto, H.; et al. Heterogeneously hybridized porous coordination polymer crystals: fabrication of heterometallic core-shell single crystals with an in-plane rotational epitaxial relationship. *Angew. Chem. Int. Ed.* **2009**, *48*, 1766–1770. [CrossRef] [PubMed]
9. Salles, F.; Maurin, G.; Serre, C.; Llewellyn, P.L.; Knoefel, C.; Choi, H.J.; Filinchuk, Y.; Oliviero, L.; Vimont, A.; Long, J.R.; et al. Multistep n-2 breathing in the metal-organic framework co(1,4-benzenedipyrazolate). *J. Am. Chem. Soc.* **2010**, *132*, 13782–13788. [CrossRef] [PubMed]
10. Furukawa, S.; Reboul, J.; Diring, S.; Sumida, K.; Kitagawa, S. Structuring of metal-organic frameworks at the mesoscopic/macroscopic scale. *Chem. Soc. Rev.* **2014**, *43*, 5700–5734. [CrossRef] [PubMed]
11. Rungtaweevoranit, B.; Zhao, Y.; Choi, K.M.; Yaghi, O.M. Cooperative effects at the interface of nanocrystalline metal-organic frameworks. *Nano Res.* **2016**, *9*, 47–58. [CrossRef]
12. Hu, M.; Belik, A.A.; Imura, M.; Yamauchi, Y. Tailored design of multiple nanoarchitectures in metal-cyanide hybrid coordination polymers. *J. Am. Chem. Soc.* **2013**, *135*, 384–391. [CrossRef] [PubMed]
13. Huo, J.; Wang, L.; Irran, E.; Yu, H.; Gao, J.; Fan, D.; Li, B.; Wang, J.; Ding, W.; Amin, A.M.; et al. Hollow ferrocenyl coordination polymer microspheres with micropores in shells prepared by ostwald ripening. *Angew. Chem. Int. Ed.* **2010**, *49*, 9237–9241. [CrossRef] [PubMed]
14. Ameloot, R.; Vermoortele, F.; Vanhove, W.; Roeffaers, M.B.J.; Sels, B.F.; De Vos, D.E. Interfacial synthesis of hollow metal-organic framework capsules demonstrating selective permeability. *Nat. Chem.* **2011**, *3*, 382–387. [CrossRef] [PubMed]
15. Brinzei, D.; Catala, L.; Mathoniere, C.; Wernsdorfer, W.; Gloter, A.; Stephan, O.; Mallah, T. Photoinduced superparamagnetism in trimetallic coordination nanoparticles. *J. Am. Chem. Soc.* **2007**, *129*, 3778–3779. [CrossRef] [PubMed]
16. Volatron, F.; Catala, L.; Riviere, E.; Gloter, A.; Stephan, O.; Mallah, T. Spin-crossover coordination nanoparticles. *Inorg. Chem.* **2008**, *47*, 6584–6586. [CrossRef] [PubMed]
17. Catala, L.; Brinzei, D.; Prado, Y.; Gloter, A.; Stephan, O.; Rogez, G.; Mallah, T. Core-multishell magnetic coordination nanoparticles: Toward multifunctionality on the nanoscale. *Angew. Chem. Int. Ed.* **2009**, *48*, 183–187. [CrossRef] [PubMed]
18. Diring, S.; Furukawa, S.; Takashima, Y.; Tsuruoka, T.; Kitagawa, S. Controlled multiscale synthesis of porous coordination polymer in nano/micro regimes. *Chem. Mater.* **2010**, *22*, 4531–4538. [CrossRef]
19. Doherty, C.M.; Buso, D.; Hill, A.J.; Furukawa, S.; Kitagawa, S.; Falcaro, P. Using functional nano- and microparticles for the preparation of metal-organic framework composites with novel properties. *Accounts Chem. Res.* **2014**, *47*, 396–405. [CrossRef] [PubMed]
20. Hu, M.; Torad, N.L.K.; Chiang, Y.-D.; Wu, K.C.W.; Yamauchi, Y. Size- and shape-controlled synthesis of Prussian Blue nanoparticles by a polyvinylpyrrolidone-assisted crystallization process. *CrystEngComm* **2012**, *14*, 3387–3396.
21. Fan, L.; Chen, H.; Xiao, D.; Wang, E. Synthesis, structure, and characterization of a new metal-organic framework containing meso-helices. *Z. Anorg. Allg. Chem.* **2013**, *639*, 558–562. [CrossRef]
22. Zhang, W.; Zhao, Y.; Malgras, V.; Ariga, K.; Yamauchi, Y.; Liu, J.; Jiang, J.S.; Hu, M. Synthesis of monocrystalline nanoframes of prussian blue analogues by controlled preferential etching. *Angew. Chem. Int. Ed.* **2016**, *55*, 8228–8234. [CrossRef] [PubMed]
23. Ariga, K.; Malgras, V.; Ji, Q.; Zakaria, M.B.; Yamauchi, Y. Coordination nanoarchitectonics at interfaces between supramolecular and materials chemistry. *Coordin. Chem. Rev.* **2016**, *320*, 139–152. [CrossRef]
24. Felts, A.C.; Andrus, M.J.; Knowles, E.S.; Quintero, P.K.; Ahir, A.R.; Risset, O.N.; Li, C.H.; Maurin, I.; Halder, G.J.; Abboud, K.A.; et al. Evidence for interface-induced strain and its influence on photomagnetism in prussian blue analogue core-shell heterostructures, RbaCob Fe(CN)(6) (c)center dot mH(2)O@KjNik Cr(CN)(6) (l)center dot nH(2)O. *J. Phys. Chem. C* **2016**, *120*, 5420–5429. [CrossRef]
25. Yue, Y.; Zhang, Z.; Binder, A.J.; Chen, J.; Jin, X.; Overbury, S.H.; Dai, S. Hierarchically superstructured prussian blue analogues: Spontaneous assembly synthesis and applications as pseudocapacitive materials. *Chem. Sus. Chem.* **2015**, *8*, 177–183. [CrossRef] [PubMed]
26. Kim, D.S.; Zakaria, M.B.; Park, M.-S.; Alowasheeir, A.; Alshehri, S.M.; Yamauchi, Y.; Kim, H. Dual-textured Prussian Blue nanocubes as sodium ion storage materials. *Electrochim. Acta* **2017**, *240*, 300–306. [CrossRef]

27. Yue, Y.; Binder, A.J.; Guo, B.; Zhang, Z.; Qiao, Z.A.; Tian, C.; Dai, S. Mesoporous Prussian blue analogues: Template-free synthesis and sodium-ion battery applications. *Angew. Chem. Int. Ed.* **2014**, *53*, 3134–3137. [CrossRef] [PubMed]
28. Lu, X.; Au, L.; McLellan, J.; Li, Z.-Y.; Marquez, M.; Xia, Y. Fabrication of cubic nanocages and nanoframes by dealloying Au/Ag alloy nanoboxes with an aqueous etchant based on $Fe(NO_3)(3)$ or NH_4OH. *Nano lett.* **2007**, *7*, 1764–1769. [CrossRef] [PubMed]
29. Mahmoud, M.A.; El-Sayed, M.A. Aggregation of gold nanoframes reduces, rather than enhances, SERS efficiency due to the trade-off of the inter- and intraparticle plasmonic fields. *Nano lett.* **2009**, *9*, 3025–3031. [CrossRef] [PubMed]
30. Mahmoud, M.A.; El-Sayed, M.A. Gold nanoframes: Very high surface plasmon fields and excellent near-infrared sensors. *J. Am. Chem. Soc.* **2010**, *132*, 12704–12710. [CrossRef] [PubMed]
31. Sui, Y.; Fu, W.; Zeng, Y.; Yang, H.; Zhang, Y.; Chen, H.; Li, Y.; Li, M.; Zou, G. Synthesis of Cu_2O nanoframes and nanocages by selective oxidative etching at room temperature. *Angew. Chem. Int. Ed.* **2010**, *49*, 4282–4285. [CrossRef] [PubMed]
32. McEachran, M.; Keogh, D.; Pietrobon, B.; Cathcart, N.; Gourevich, I.; Coombs, N.; Kitaev, V. Ultrathin gold nanoframes through surfactant-free templating of faceted pentagonal silver nanoparticles. *J. Am. Chem. Soc.* **2011**, *133*, 8066–8069. [CrossRef] [PubMed]
33. Hong, X.; Wang, D.; Cai, S.; Rong, H.; Li, Y. Single-crystalline octahedral au-ag nanoframes. *J. Am. Chem. Soc.* **2012**, *134*, 18165–18168. [CrossRef] [PubMed]
34. Xie, S.; Lu, N.; Xie, Z.; Wang, J.; Kim, M.J.; Xia, Y. Synthesis of Pd-Rh core-frame concave nanocubes and their conversion to rh cubic nanoframes by selective etching of the Pd cores. *Angew. Chem. Int. Ed.* **2012**, *51*, 10266–10270. [CrossRef] [PubMed]
35. Chen, C.; Kang, Y.; Huo, Z.; Zhu, Z.; Huang, W.; Xin, H.L.; Snyder, J.D.; Li, D.; Herron, J.A.; Mavrikakis, M.; et al. Highly crystalline multimetallic nanoframes with three-dimensional electrocatalytic surfaces. *Science* **2014**, *343*, 1339–1343. [CrossRef] [PubMed]
36. Zhang, L.; Roling, L.T.; Wang, X.; Vara, M.; Chi, M.; Liu, J.; Choi, S.-I.; Park, J.; Herron, J.A.; Xie, Z.; et al. Platinum-based nanocages with subnanometer-thick walls and well-defined, controllable facets. *Science* **2015**, *349*, 412–416. [CrossRef] [PubMed]
37. Wessells, C.D.; McDowell, M.T.; Peddada, S.V.; Pasta, M.; Huggins, R.A.; Cui, Y. Tunable reaction potentials in open framework nanoparticle battery electrodes for grid-scale energy storage. *Acs Nano* **2012**, *6*, 1688–1694. [CrossRef] [PubMed]
38. Pasta, M.; Wessells, C.D.; Liu, N.; Nelson, J.; McDowell, M.T.; Huggins, R.A.; Toney, M.F.; Cui, Y. Full open-framework batteries for stationary energy storage. *Nat. Commun.* **2014**, *5*, 10. [CrossRef] [PubMed]
39. Wang, R.Y.; Wessells, C.D.; Huggins, R.A.; Cui, Y. Highly reversible open framework nanoscale electrodes for divalent ion batteries. *Nano lett.* **2013**, *13*, 5748–5752. [CrossRef] [PubMed]
40. Lee, H.-W.; Wang, R.Y.; Pasta, M.; Lee, S.W.; Liu, N.; Cui, Y. Manganese hexacyanomanganate open framework as a high-capacity positive electrode material for sodium-ion batteries. *Nat. Commun.* **2014**, *5*. [CrossRef] [PubMed]
41. Chae, M.S.; Hyoung, J.; Jang, M.; Lee, H.; Hong, S.-T. Potassium nickel hexacyanoferrate as a high-voltage cathode material for nonaqueous magnesium-ion batteries. *J. Power Sources* **2017**, *363*, 269–276. [CrossRef]
42. Okubo, M.; Li, C.H.; Talham, D.R. High rate sodium ion insertion into core-shell nanoparticles of Prussian blue analogues. *Chem. Commun.* **2014**, *50*, 1353–1355. [CrossRef] [PubMed]
43. Tang, W.; Zhu, Y.; Hou, Y.; Liu, L.; Wu, Y.; Loh, K.P.; Zhang, H.; Zhu, K. Aqueous rechargeable lithium batteries as an energy storage system of superfast charging. *Energ. Environ. Sci.* **2013**, *6*, 2093–2104. [CrossRef]
44. Zhao, F.; Wang, Y.; Xu, X.; Liu, Y.; Song, R.; Lu, G.; Li, Y. Cobalt hexacyanoferrate nanoparticles as a high-rate and ultra-stable supercapacitor electrode material. *ACS Appl. Mater. Inter.* **2014**, *6*, 11007–11012. [CrossRef] [PubMed]
45. Pasta, M.; Wessells, C.D.; Huggins, R.A.; Cui, Y. A high-rate and long cycle life aqueous electrolyte battery for grid-scale energy storage. *Nat. Commun.* **2012**, *3*, 1149–1155. [CrossRef] [PubMed]
46. Wessells, C.D.; Huggins, R.A.; Cui, Y. Copper hexacyanoferrate battery electrodes with long cycle life and high power. *Nat. Commun.* **2011**, *2*, 550–554. [CrossRef] [PubMed]

47. Chen, R.; Huang, Y.; Xie, M.; Zhang, Q.; Zhang, X.; Li, L.; Wu, F. Preparation of Prussian Blue submicron particles with a pore structure by two-step optimization for Na-ion battery cathodes. *ACS Appl. Mater. Inter.* **2016**, *8*, 16078–16086. [CrossRef] [PubMed]
48. Wang, L.; Lu, Y.; Liu, J.; Xu, M.; Cheng, J.; Zhang, D.; Goodenough, J.B. A superior low-cost cathode for a Na-ion battery. *Angew. Chem. Int. Ed.* **2013**, *52*, 1964–1967. [CrossRef] [PubMed]
49. You, Y.; Wu, X.-L.; Yin, Y.-X.; Guo, Y.-G. High-quality Prussian blue crystals as superior cathode materials for room-temperature sodium-ion batteries. *Energ. Environ. Sci.* **2014**, *7*, 1643–1647. [CrossRef]
50. Liu, Y.; Qiao, Y.; Zhang, W.; Li, Z.; Ji, X.; Miao, L.; Yuan, L.; Hu, X.; Huang, Y. Sodium storage in Na-rich NaxFeFe (CN)(6) nanocubes. *Nano Energy* **2015**, *12*, 386–393. [CrossRef]
51. You, Y.; Yu, X.; Yin, Y.; Nam, K.-W.; Guo, Y.-G. Sodium iron hexacyanoferrate with high Na content as a Na-rich cathode material for Na-ion batteries. *Nano Res.* **2014**, *8*, 117–128. [CrossRef]
52. Wessells, C.D.; Peddada, S.V.; Huggins, R.A.; Cui, Y. Nickel hexacyanoferrate nanoparticle electrodes for aqueous sodium and potassium ion batteries. *Nano Lett.* **2011**, *11*, 5421–5425. [CrossRef] [PubMed]
53. Targholi, E.; Mousavi-Khoshdel, S.M.; Rahmanifara, M.; Yahya, M.Z.A. Cu- and Fe-hexacyanoferrate as cathode materials for Potassium ion battery: A First-principles study. *Chem. Phys. Lett.* **2017**, *687*, 244–249. [CrossRef]
54. Lu, Y.; Wang, L.; Cheng, J.; Goodenough, J.B. Prussian blue: A new framework of electrode materials for sodium batteries. *Chem. Commun.* **2012**, *48*, 6544–6546. [CrossRef] [PubMed]
55. Wessells, C.D.; Peddada, S.V.; McDowell, M.T.; Huggins, R.A.; Cui, Y. The effect of insertion species on nanostructured open framework hexacyanoferrate battery electrodes. *J. Electrochem. Soc.* **2012**, *159*, 98–103. [CrossRef]
56. Kim, D.; Hwang, T.; Lim, J.-M.; Park, M.-S.; Cho, M.; Cho, K. Hexacyanometallates for sodium-ion batteries: Insights into higher redox potentials using d electronic spin configurations. *Phys. Chem. Chem.l Phys.* **2017**, *19*, 10443–10452. [CrossRef] [PubMed]
57. Liu, Y.; He, D.; Han, R.; Wei, G.; Qiao, Y. Nanostructured potassium and sodium ion incorporated Prussian blue frameworks as cathode materials for sodium-ion batteries. *Chem. Commun.* **2017**, *53*, 5569–5572. [CrossRef] [PubMed]
58. Liang, G.; Xu, J.; Wang, X. Synthesis and characterization of organometallic coordination polymer nanoshells of Prussian blue using miniemulsion periphery polymerization (MEPP). *J. Am. Chem. Soc.* **2009**, *131*, 5378–5379. [CrossRef] [PubMed]
59. McHale, R.; Ghasdian, N.; Liu, Y.; Ward, M.B.; Hondow, N.S.; Wang, H.; Miao, Y.; Brydson, R.; Wang, X. Prussian blue coordination polymer nanobox synthesis using miniemulsion periphery polymerization (MEPP). *Chem. Commun.* **2010**, *46*, 4574–4576. [CrossRef] [PubMed]
60. Hu, M.; Jiang, J.S. Facile synthesis of air-stable Prussian white microcubes via a hydrothermal method. *Mater. Res. Bull.* **2011**, *46*, 702–707. [CrossRef]
61. McHale, R.; Liu, Y.; Ghasdian, N.; Hondow, N.S.; Ye, S.; Lu, Y.; Brydson, R.; Wang, X. Dual lanthanide role in the designed synthesis of hollow metal coordination (Prussian Blue analogue) nanocages with large internal cavity and mesoporous cage. *Nanoscale* **2011**, *3*, 3685–3694. [CrossRef] [PubMed]
62. Roy, X.; Hui, J.K.H.; Rabnawaz, M.; Liu, G.; MacLachlan, M.J. Prussian blue nanocontainers: selectively permeable hollow metal-organic capsules from block lonomer emulsion-induced assembly. *J. Am. Chem. Soc.* **2011**, *133*, 8420–8423. [CrossRef] [PubMed]
63. Risset, O.N.; Knowles, E.S.; Ma, S.; Meisel, M.W.; Talham, D.R. RbjMk Fe(CN)(6) (l) (M = Co, Ni) Prussian blue analogue hollow nanocubes: A new example of a multilevel pore system. *Chem. Mater.* **2013**, *25*, 42–47. [CrossRef]
64. Shen, Q.; Jiang, J.; Fan, M.; Liu, S.; Wang, L.; Fan, Q.; Huang, W. Prussian blue hollow nanostructures: Sacrificial template synthesis and application in hydrogen peroxide sensing. *J. Electroanal. Chem.* **2014**, *712*, 132–138. [CrossRef]
65. Hu, M.; Jiang, J.-S.; Zeng, Y. Prussian blue microcrystals prepared by selective etching and their conversion to mesoporous magnetic iron(III) oxides. *Chem. Commun.* **2010**, *46*, 1133–1135. [CrossRef] [PubMed]
66. Hu, M.; Torad, N.L.; Yamauchi, Y. Preparation of Various Prussian Blue analogue hollow nanocubes with single crystalline shells. *Eur. J. Inorg. Chem.* **2012**, *30*, 4795–4799. [CrossRef]
67. Lee, S.-H.; Huh, Y.-D. Preferential evolution of Prussian blue's morphology from cube to hexapod. *B. Kor. Chem. Soc.* **2012**, *33*, 1078–1080. [CrossRef]

68. Song, Y.; He, J.; Wu, H.; Li, X.; Yu, J.; Zhang, Y.; Wang, L. Preparation of porous hollow CoOx nanocubes via chemical etching prussian blue analogue for glucose sensing. *Electrochim. Acta* **2015**, *182*, 165–172. [CrossRef]
69. Han, L.; Yu, T.; Lei, W.; Liu, W.; Feng, K.; Ding, Y.; Jiang, G.; Xu, P.; Chen, Z. Nitrogen-doped carbon nanocones encapsulating with nickel-cobalt mixed phosphides for enhanced hydrogen evolution reaction. *J. Mater. Chem. A* **2017**, *5*, 16568–16572. [CrossRef]
70. Liu, Y.; Wei, G.; Ma, M.; Qiao, Y. Role of acid in tailoring Prussian blue as cathode for high-performance sodium-ion battery. *Chem. Eur. J.* **2017**, *23*, 15991–15996. [CrossRef] [PubMed]
71. Zhang, G.; Xu, X.; Ji, Q.; Liu, R.; Liu, H.; Qiu, J.; Li, J. Porous nanobimetallic Fe-Mn cubes with high valent mn and highly efficient removal of arsenic(III). *ACS Appl. Mater. Inter.* **2017**, *9*, 14868–14877. [CrossRef] [PubMed]
72. Hu, M.; Furukawa, S.; Ohtani, R.; Sukegawa, H.; Nemoto, Y.; Reboul, J.; Kitagawa, S.; Yamauchi, Y. Synthesis of Prussian blue nanoparticles with a hollow interior by controlled chemical etching. *Angew. Chem. Int. Ed.* **2012**, *51*, 984–988. [CrossRef] [PubMed]
73. Yang, J.; Zhang, F.; Lu, H.; Hong, X.; Jiang, H.; Wu, Y.; Li, Y. Hollow Zn/Co ZIF particles derived from core-shell zif-67@zif-8 as selective catalyst for the semi-hydrogenation of acetylene. *Angew. Chem. Int. Ed.* **2015**, *54*, 10889–10893. [CrossRef] [PubMed]
74. Ren, W.; Qin, M.; Zhu, Z.; Yan, M.; Li, Q.; Zhang, L.; Liu, D.; Mai, L. Activation of sodium storage sites in prussian blue analogues via surface etching. *Nano lett.* **2017**, *17*, 4713–4718. [CrossRef] [PubMed]
75. Han, L.; Yu, X.-Y.; Lou, X.W. Formation of Prussian-blue-analog nanocages via a direct etching method and their conversion into Ni-Co-Mixed oxide for enhanced oxygen evolution. *Adv. Mater.* **2016**, *28*, 4601–4605. [CrossRef] [PubMed]
76. Ahirwar, P.; Clark, S.P.R.; Patel, V.; Rotter, T.J.; Hains, C.; Albrecht, A.; Dawson, L.R.; Balakrishnan, G. Perforated (In)GaSb quantum wells on GaSb substrates through the use of As(2) based in situ etches. *J. Vac. Sci. Technol. B* **2011**, *29*. [CrossRef]
77. Li, G.; Li, Y.; Li, Y.; Peng, H.; Chen, K. Polyaniline nanorings and flat hollow capsules synthesized by in situ sacrificial oxidative templates. *Macromolecules* **2011**, *44*, 9319–9323. [CrossRef]
78. Yang, K.C.; Jeon, M.H.; Yeom, G.Y. A study on the etching characteristics of magnetic tunneling junction materials using DC pulse-biased inductively coupled plasmas. *Jpn. J. Appl. Phys.* **2015**, *54*. [CrossRef]
79. Zhang, C.; Zhou, Y.; Zhang, Y.; Zhao, S.; Fang, J.; Sheng, X.; Zhang, H. A novel hierarchical TiO2@Pt@mSiO(2) hollow nanocatalyst with enhanced thermal stability. *J. Alloy. Compd.* **2017**, *701*, 780–787. [CrossRef]
80. Chen, L.; Bao, J.L.; Dong, X.; Truhlar, D.G.; Wang, Y.; Wang, C.; Xia, Y. Aqueous Mg-Ion battery based on polyimide anode and Prussian blue cathode. *ACS Energy Lett.* **2017**, *2*, 1115–1121. [CrossRef]
81. Wu, X.; Sun, M.; Guo, S.; Qian, J.; Liu, Y.; Cao, Y.; Ai, X.; Yang, H. Vacancy-free Prussian blue nanocrystals with high capacity and superior cyclability for aqueous sodium-ion batteries. *Chem. Nano Mat.* **2015**, *1*, 188–193. [CrossRef]
82. Whitacre, J.F.; Tevar, A.; Sharma, S. $Na_4Mn_9O_{18}$ as a positive electrode material for an aqueous electrolyte sodium-ion energy storage device. *Electrochem. Commun.* **2010**, *12*, 463–466. [CrossRef]
83. Wu, X.; Cao, Y.; Ai, X.; Qian, J.; Yang, H. A low-cost and environmentally benign aqueous rechargeable sodium-ion battery based on $NaTi_2(PO_4)_3$–$Na_2NiFe(CN)_6$ intercalation chemistry. *Electrochem. Commun.* **2013**, *31*, 145–148. [CrossRef]
84. Luo, J.-Y.; Cui, W.-J.; He, P.; Xia, Y.-Y. Raising the cycling stability of aqueous lithium-ion batteries by eliminating oxygen in the electrolyte. *Nat. Chem.* **2010**, *2*, 760–765. [CrossRef] [PubMed]
85. Hu, M.; Ishihara, S.; Ariga, K.; Imura, M.; Yamauchi, Y. Kinetically controlled crystallization for synthesis of monodispersed coordination polymer nanocubes and their self-assembly to periodic arrangements. *Chem. Eur. J.* **2013**, *19*, 1882–1885. [CrossRef] [PubMed]
86. Widmann, A.; Kahlert, H.; Wulff, H.; Scholz, F. Electrochemical and mechanochemical formation of solid solutions of potassium copper(II)/zinc(II) hexacyanocobaltate(III)/hexacyanoferrate(III) KCu_xZn_{1-x} hcc (x) hcf (1-x). *J. Solid State Electr.* **2005**, *9*, 380–389. [CrossRef]
87. Kulesza, P.J.; Malik, M.A.; Denca, A.; Strojek, J. In situ FT-IR/ATR spectroelectrochemistry of Prussian blue in the solid state. *Anal. Chem.* **1996**, *68*, 2442–2446. [CrossRef]
88. Hung, T.-F.; Chou, H.-L.; Yeh, Y.-W.; Chang, W.-S.; Yang, C.-C. Combined experimental and computational studies of a na2ni1-xcuxfe(cn)(6) cathode with tunable potential for aqueous rechargeable sodium-ion batteries. *Chem. Europe. J.* **2015**, *21*, 15686–15691. [CrossRef] [PubMed]

89. Hung, T.-F.; Cheng, W.-J.; Chang, W.-S.; Yang, C.-C.; Shen, C.-C.; Kuo, Y.-L. Ascorbic acid-assisted synthesis of mesoporous sodium vanadium phosphate nanoparticles with highly sp(2)-coordinated carbon coatings as efficient cathode materials for rechargeable sodium-ion batteries. *Chem. Eur. J.* **2016**, *22*, 10620–10626. [CrossRef] [PubMed]
90. You, Y.; Wu, X.-L.; Yin, Y.-X.; Guo, Y.-G. A zero-strain insertion cathode material of nickel ferricyanide for sodium-ion batteries. *J. Mater. Chem. A* **2013**, *1*, 14061–14065. [CrossRef]